J MATER RES TECHNOL. 2020;9(6):13054–13066

Available online at www.sciencedirect.com

jmr&t Journal of Materials Research and Technology

https://www.journals.elsevier.com/journal-of-materials-research-and-technology

Original Article

Synthesis and application of rice husk silica nanoparticles for chemical enhanced oil recovery

Augustine Agi[a,b], *Radzuan Junin*[a,b,*], *Mohd Zaidi Jaafar*[a,b,*], *Rahmat Mohsin*[b], *Agus Arsad*[b], *Afeez Gbadamosi*[c], *Cheo Kiew Fung*[a], *Jeffrey Gbonhinbor*[d]

[a] *Department of Petroleum Engineering, School of Chemical and Energy Engineering, Faculty of Engineering, Universiti Teknologi Malaysia, Johor Bahru, 81310, Malaysia*

[b] *Drilling and Production Enhanced Research Group, Institute for Oil and Gas (IFOG), Universiti Teknologi Malaysia, Johor Bahru, 81310, Malaysia*

[c] *Department of Chemical and Petroleum Engineering, College of Engineering, Afe Babalola University, PMB 5454, Ado-Ekiti, Ekiti State, Nigeria*

[d] *Department of Petroleum Engineering, Faculty of Chemical Engineering, Niger Delta University, Wilberforce Island Amassoma, Bayelsa State, Nigeria*

ARTICLE INFO

Article history:
Received 15 May 2020
Accepted 28 August 2020
Available online 25 September 2020

Keywords:
Rice husk
Nanoparticles
Polyacrylamide, Interfacial tension,
Rheology, Enhanced oil recovery

ABSTRACT

Silica (SiO_2) nanoparticles were synthesized from rice husk (RH) via wet milling method and evaluated for enhanced oil recovery (EOR) applications. Physical properties of RH-SiO_2 nanoparticles (RH-SNP) with its size distribution were explored through field emission scanning electron microscopy (FESEM) and dynamic light scattering (DLS). Stability, functional groups and purity of RH-SNP were determined by zeta potential, Fourier-transform infrared (FTIR) spectroscopy and X-ray diffraction (XRD), respectively. Effect of RH-SNP on the precipitation and thermal degradation of oilfield polyacrylamide (HPAM) was studied using Brookfield RST rheometer. Interfacial tension (IFT) properties of RH-SiO_2 polymeric nanofluid (RH-SPNF) at interface of oil and water (O/W) were investigated using Easy-Dyne KRUSS tensiometer. Subsequently, oil displacement efficiency of RH-SPNF was determined and compared with oilfield HPAM at reservoir conditions using Fars EOR high-pressure high-temperature (HPHT) core flooding equipment. The wet milling method was effective in producing RH-SNP of size ranges 43.9–59.5 nm with a purity of 98% through the mechanism of nucleation, Brownian motion and coalescence. Rheological results show that RH-SNP inhibited the precipitation and thermal degradation of oilfield HPAM. IFT of RH-SPNF showed a monotonic tendency as temperature increased. HPAM and RH-SPNF flooding showed an incremental oil recovery of approximately 10% and 24%, respectively. Emulsion generated using RH-SPNF shows higher stability and resistance to coalescence. Finally, mobility ratio

* *Corresponding author.*
E-mails: r-radzuan@utm.my (R. Junin), mzaidi@utm.my (M.Z. Jaafar).

https://doi.org/10.1016/j.jmrt.2020.08.112

of water flooding approaches unity faster, compared to HPAM and RH-SPNF. Overall, the low energy utilization, use of low-cost and benign raw material make RH-SNP and the extraction method an appropriate substitute to commercially available SiO_2 nanoparticles.

1. Introduction

Increased energy consumption in juxtaposition to dwindling oil reserves has continued to pose a huge problem to oil industry. Oil production from active reservoirs continues to decline, coupled with lack of new abundant reserves. Literature shows that two-third of the original-oil-in-place (OOIP) is still trapped in the reservoir after initial recovery and water flooding [1,2]. Hence, enhanced oil recovery (EOR) could play a vital role in meeting the increased energy demand. EOR processes are used to improve the productivity of the existing fields with the aim of recovering the trapped oil in reservoirs [3].

Hitherto, numerous EOR methods such as gas, thermal and chemical (alkali, surfactants and polymers) have been developed and evaluated to overcome the low oil recovery efficiency. Chemical EOR (CEOR) technique is deemed highly favourable due to its better efficiency and reasonable capital cost. EOR chemicals such as alkali and surfactants can reduce interfacial tension (IFT) by altering rock/fluid interface in the reservoir. Besides, they can also alter wettability between oil-rock-brine interface [1]. On the other hand, polymer flooding is widely applied to increase viscosity of the injectant and consequently improve the mobility of the reservoir fluids. Hence, viscous fingering is minimised and/or eradicated, conformance control is enhanced and higher sweep efficiency is achieved. Field results have shown that the use of polymer flooding can recover additional 5-30% OOIP [4,5].

Hydrolysed polyacrylamide (HPAM) is the most widely used polymer in oilfields because of inexpensive handling cost, relatively resistant to bacterial attack, high solubility in water and disproportionate permeability reduction characteristics [6]. However, with variation in crude oil properties and harsh environmental conditions of the reservoir, HPAM does not perform appropriately. Therefore, various studies are being carried out to improve the limitations of HPAM against high temperature and high salinity reservoir conditions.

Recently, researchers have reported the use of nanofluid in CEOR process. Nanofluid, which is the synergy of base fluid with nanoparticles, has the advantages of being more tolerant to high salinity, high temperature, longer stability, less plugging and retention in reservoir. The recent trend in nanotechnology has focused on incorporating polymers with nanoparticles to produce fluids with distinct characteristics of the formulated polymeric nanofluids. Various studies have reported the use of silica (SiO_2) [7–9], titanium dioxide [10], graphene oxide [11], and aluminium oxide [12,13] nanoparticles to improve the rheology, and viscoelastic properties of HPAM. They reported that the presence of nanoparticles significantly improved the properties of HPAM at harsh reservoir conditions.

Lately, bio-based materials are attracting interest in diverse fields because of their availability, low cost, and benign nature [14,15]. A research of new bio-based materials with potential application in energy storage device has proven that cellulose derivate can be easily incorporated in various polymeric materials [16–18]. Their chemical bonding can greatly enhance and accelerate energy transition and boost the use of abundant elements for large scale production [19–21]. However, SiO_2 nanoparticles are the most widely used in EOR application. This is because about 99.8% of SiO_2 nanoparticles are silicon dioxide, which is the main component of sandstone, making it the most abundant naturally occurring compound on earth. Furthermore, SiO_2 nanoparticles can be easily produced and their chemical behaviour can be easily controlled by surface modification for specific application such as EOR.

Despite the extensive investigation from previous research on SiO_2 nanoparticles for EOR application, there are still some challenges in the field owing to cost and huge environmental problems [22,23]. Mining of SiO_2 sand involves topsoil removal and excavation of sand. Hence, the mined SiO_2 is often associated with impurities such as feldspar and clay, which need further purification. The purification of SiO_2 sand leaves deleterious contaminants such as boron, arsenic and fluorine which affect their industrial applicability [24]. As such, SiO_2 nanoparticles from renewable materials have been sought after to replace the existing ones [25,26]. Hence, this study extends the frontier of research by synthesizing SiO_2 nanoparticles from rice husk (RH) using wet milling method and thereafter evaluating it for their EOR applications. RH is an abundantly available and renewable agriculture by-product from the first stage of rice milling.

In this study, SiO_2 nanoparticles were synthesized from RH. The physical properties of RH-SiO_2 nanoparticles (RH-SNP), including their size distribution, were investigated. The stability, functional groups and purity of the RH-SNP were determined. Furthermore, the effect of RH-SNP on the precipitation and thermal degradation of oilfield HPAM was studied. Additionally, the IFT properties of the RH-SiO_2 polymeric nanofluid (RH-SPNF) at the interface of oil-water (O/W) were investigated. Subsequently, oil displacement efficiency of RH-SPNF was determined and compared with oilfield HPAM at reservoir conditions. Finally, the energy utilization and expenditure of the process and materials were examined in comparison to traditional methods.

2. Materials and methods

2.1. *Materials*

RH was obtained from Kilang Beras Rice Mill, Bagan Serai, Perak, Malaysia. HPAM with degree of hydrolysis 25 mol%,

Table 1 – Properties of sandstone core

Diameter (cm)	Length (cm)	Bulk volume (cm^3)	Pore volume (cm^3)	Porosity (%)	Permeability (mD)
3.7	9.8	100.37	17.00	16.9	201

molecular weight of 20×10^6 Dalton was obtained from SNF Floerger, Paris. Sodium chloride (NaCl) with 99% purity and molecular weight 58.44 g/mol was obtained from Merck group. Molecular biology grade ethanol with purity of 96% was purchased from Fisher BioReagents. An intermediate crude oil from an oilfield in Sarawak, Malaysia (density of 0.82 g/mL @25 °C, API of 37.7 and viscosity of 10 mPa s @25 °C) was used for the experiments. Three mid-permeability sandstone cores from the same outcrop were utilized for core flooding test. The physical properties of the sandstone cores are shown in Table 1. The X-ray diffraction (XRD) of the core (Figure S1, supporting information) reveals that the samples are mainly quartz (98.9%) and illite (1.1%).

2.2. Methods

2.2.1. Synthesis of RH-SNP

RH was sieved and treated using an electric furnace (Thermolyne 30400 Laboratory Furnace: Barnstead, USA) at 700 °C for 4 h. This is to decrease the amount of carbonaceous material present in the RH and to increase SiO_2 content. A two-stage ball milling process was used to reduce the particles to nano size. A planetary ball mill machine DECO-PBM-V-2L-A; DECO, China containing a 250 mL tungsten carbide grinding jar was loaded with 150 mL of tungsten carbide balls and 85 mL of RH. It was milled for 2 h at 400 rpm; this was done to achieve homogenous particles size. The sample was then dispersed in ethanol to prevent agglomeration of the particles. Wet milling was performed for 5 h at 400 rpm to achieve nano sizes. The sample was collected and dried in an oven at 80 °C for 17 h. The energy and cost were estimated:

$$E = Pt \quad (1)$$

$$cost = E\ (cost\ 1kwh) \quad (2)$$

where E is electrical energy (kwh), P is power of electrical appliance (kw), t is time of electricity consumption (h).

2.2.2. RH-SPNF preparation

RH-SPNF was made by a two-stage technique. 0.1 wt.% (critical nanoparticle concentration) [12,27], of RH-SNP was dispersed in deionized water (DIW) and sonicated for 35 min. to form a homogenous dispersion. HPAM of 0.1 wt.% (critical concentration of HPAM solution) [12], was added to the nanofluids dispersion and agitated for 23 h on a stirrer. To investigate the impact of salinity on RH-SPNF, NaCl with different concentrations (0.9–2.2 wt.%) was added to the polymeric nanofluid suspension and stirred for 24 h. The salinity range depicts a Malay Basin oil reservoir salinity [28].

2.2.3. Morphology and surface structure

Field emission scanning electron microscopy (FESEM) with energy dispersive X-Ray (EDX) (Ultra, Zeiss, Germany) was used to determine the surface structure of RH, RH-SNP and elemental composition of the RH-SNP. The FESEM test was conducted with a magnification of 30.0 KX through an aperture size of 30.0 μm and zoomed to 500 nm. Prior to image acquisition, the samples were coated with gold particles in order to enhance the visibility of the image.

2.2.4. Particle size analysis and surface charge

Light scattering instrument (Anton Paar Litesizer™ 500) with a particle size range of 1 nm to 10 μm for particle analysis was used to examine the size distribution and surface charge of the RH-SNP. The RH-SNP was dissolved in distilled water (DW) (0.1%) and moved to omega cuvette for analysis. The analysis was carried out at a back-scattering angle of 170° at 25 °C. The refractive index of water was 1.3303 and the viscosity of water was 0.8903 mPa s.

2.2.5. XRD analysis

XRD of RH-SNP was evaluated using SmartLab; Rigaku, Japan, with a radiation of 40 kV and 30 mA. XRD spectra were spotted at two-theta scanning range of 5–100° at 8.2551 °/min. The relative crystallinity (RC) was quantitatively calculated using the method of Nara and Komiya [29]:

$$RC\ (\%) = \frac{A_C}{A_a + A_c} \quad (3)$$

where A_c is crystalline area and A_a is amorphous area on the X-ray diffractogram.

2.2.6. Fourier-transform infrared spectroscopy (FTIR) analysis

FTIR analysis was used to confirm the RH-SNP. Shimadzu IR Tracer-100 was used to determine the FTIR spectra of the RH-SNP. Dry RH-SNP was added to potassium bromide (KBr) before it was placed in a sample bearer. FTIR was achieved at a range of 600–4000 cm^{-1}.

2.2.7. Rheological analysis

The rheology of RH-SPNF and HPAM was determined using Brookfield RST rheometer. The rheometer is composed of temperature control connected to water bath for high temperature conditions. All the measurements were carried out at 1–1000 s^{-1} (shear rate) at a temperature range of 26–80 °C. For repeatability, the experiments were conducted in triplicate and the average values were reported.

2.2.8. IFT determination

The IFT between RH-SPNF and oil was determined with Easy Dyne tensiometer (K20) by Kruss GmbH, Germany. The tensiometer has a water-bath connected to control temperature of the tensiometer. IFT of RH-SPNF (0.2 wt%) as a function of NaCl concentration (2.2 wt%) and temperature (26 –80 °C) was determined. All the experiments were repeated once, and the average values were reported.

2.2.9. *Core flooding test*

The oil displacement test was investigated using a high-pressure high-temperature (HPHT) apparatus manufactured by Fars EOR technologies (Figure S2). It consists of a furnace for temperature regulation, four accumulators for injecting fluid and a compartment for holding the core. It has a temperature limit of 150 °C and pressure capacity of 6000 psi. Three identical mid-permeability core samples from the same location were utilized for displacement test (Table 1). Core samples were washed with toluene in a Soxhlet distillation extractor column before and after each use. The cores were subsequently dried for 24 h at 95 °C in an oven. Oil displacement tests were executed to determine the oil recovery efficiency of RH-SPNF and HPAM. To simulate the reservoir condition of a typical Sarawak oilfield, the equipment was pressured to 3000 psi (with a back pressure of 100 psi) and oven temperature raised to 120 °C. After vacuuming, the system was saturated with 2.2 wt% of synthetic brine and flooded with oil until connate water was achieved. ISCO pump was utilized in pumping injectants from accumulators to the equipment. Crude oil was introduced into the core at 0.5 mL/min and aged for 24 h to achieve stability. Consequently, water was injected at a constant flow rate until breakthrough occurred. Then, 0.5 PV consisting of 0.2 wt.% of RH-SPNF and HPAM was injected to recover the bypassed oil. Chase water (0.5 PV) was later injected to recover any remaining oil. All the experiments were conducted in duplicate and the average values reported.

3. Results and Discussion

3.1. *Morphology and surface structure*

The RH was incinerated (Figure S3a) and thermally treated (Figure S3b) to remove excess salt and organic matter. Heating RH above 400 °C eliminates element which might be in the RH, thereby purifying the silicon content and making it more soluble [30]. The alcohol added to the dry RH during the milling process (Figure S4a) acted in place of surfactant as micelle maker [31]. This helped to control the size of RH-SNP (Figure S4b) from agglomeration and modified the surface during wet milling.

The FESEM of the RH (Fig. 1a) reveals a heterogenous material with a rough and irregular shape with mean diameter of 3 μm. The roughness of RH was due to release of organic matter during thermal heating. The sizes of the RH reduced to nanosize ranges of 43.9–59 nm (Fig. 2b) after synthesis. The micellar environment generated by the alcohol during synthesis was effective in controlling the sizes as all the RH-SNP were less than 100 nm. However, the sizes were not uniform, which was coherent with earlier work Rovani et al. [30] where they reported nonuniform silica nanoparticles from sugar cane. The large particle sizes in Fig. 1b could be due to Oswaldo ripening, as smaller nanoparticles are dissolved and redeposited onto larger particles, thus allowing for the formation of monodisperse particles [32]. The EDX (Fig. 2) shows the major elements silicon (Si), carbon (C) and oxygen (O). Minor elements iron, chromium, potassium, nickel, calcium, manganese, magnesium and phosphorous were also present. The presence of Si and O confirms the existence of SiO_2, whereas the presence of C shows the biological origin of the sample. The higher energy peak intensity of Si might be because of energy peak overlap due to cross excitation of X-ray signal coming from different particles [33,34].

3.2. *Mechanisms of nanoparticles formation by wet milling*

The addition of alcohol to the dry RH acts as a liquid binder and stabilizing agent. Thereafter, it spreads on the surface of the agitated RH powder bed and wetted the particles as depicted in Figure S5. The alcohol penetrated the RH powder bed by capillary action. The wetted particles formed a nucleus resulting in nucleation of individual particles coated with a layer of liquid or a closely packed, partially or fully saturated nuclei granules. Thereafter, the RH particles began to collide with each other, the mill ball and the walls of the mill in a Brownian motion leading to densification. Densification forced the

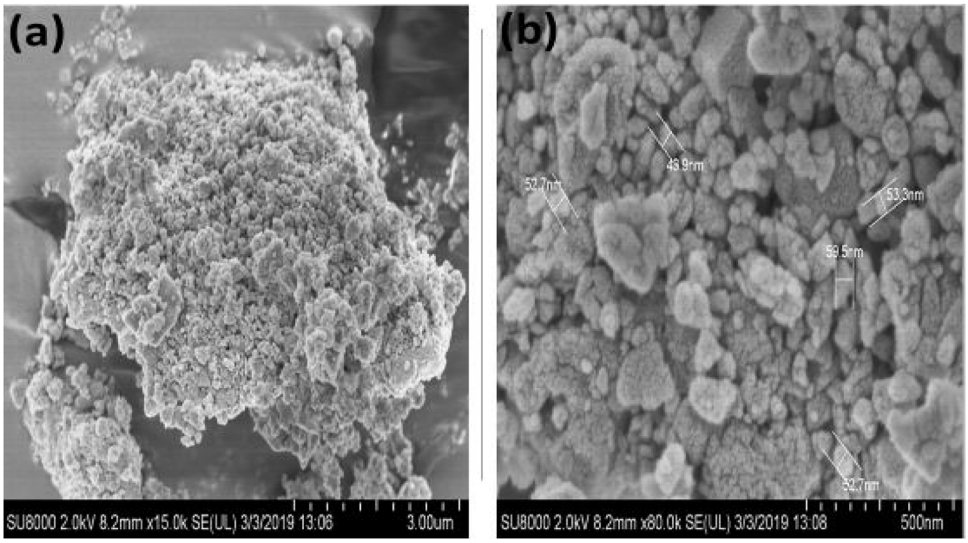

Fig. 1 – FESEM image of (a) RH before synthesis, (b) RH-SNP after synthesis.

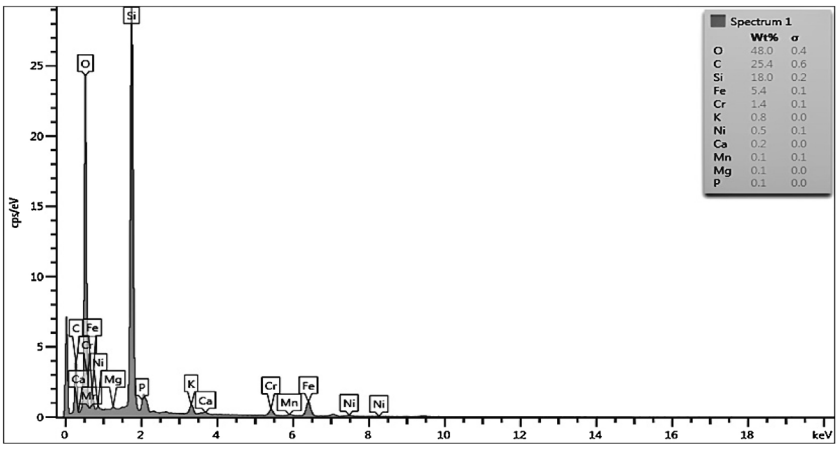

Fig. 2 – EDX of RH-SNP showing the major and minor elements.

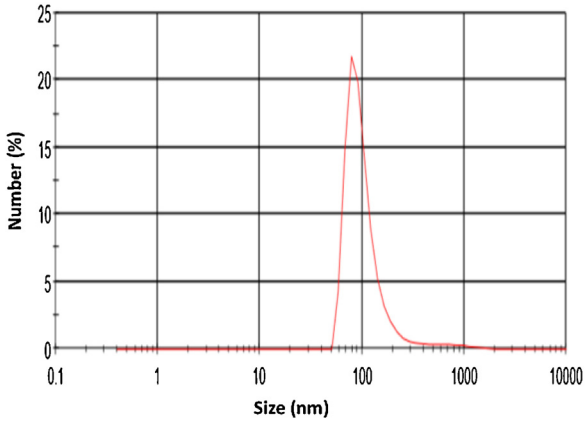

Fig. 3 – Particles size of RH-SNP showing monomodal distribution.

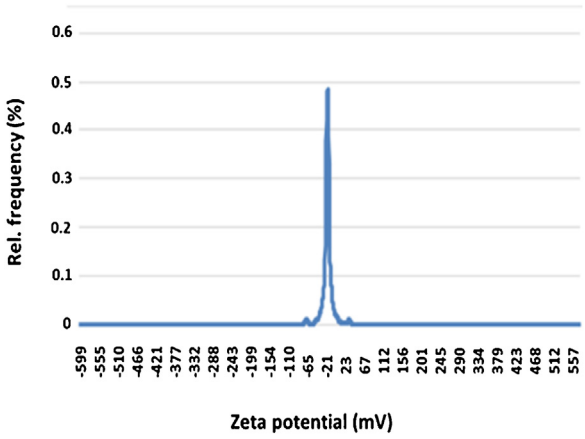

Fig. 4 – Zeta potential of RH-SNP solution at ambient temperature

liquid to migrate to the surface resulting to coalescence and growth of the RH particles (Figure S5). As the RH particles continue to collide with each other, mill ball and walls of the mill, consolidation and binding occurs, leading to deformation of the RH particles and rapid growth [35]. The collision continued until the collision force exceeds the critical value the granule can hold and due to the high shear forces exhibited in the ball mill. Thereafter, the RH particle collapse and breaks releasing nano size particles of RH-SiO_2 as seen in Figure S5.

3.3. *Particle size analysis and surface charge of RH-SNP*

RH-SNP size distribution (Fig. 3) shows a monomodal distribution with size ranges of 50-70 nm. The particle size distribution is consistent with FESEM result (Fig. 1b). However, it shows larger RH-SNP sizes compared to the FESEM result. This is because the hydrodynamic size measured by the DLS is the size of the hypothetical hard sphere that diffuses similarly to the particles being measured [31]. Hence, the diameter calculated is only indicative of the apparent size of the dynamic hydrated/solvated particles. It does not signify the actual size of monodispersed RH-SNP. Therefore, the reported hydrodynamic diameter cannot be used as approximation of size but rather for comparison [31]. The small sizes of the particles demonstrate the ability of the particles to deform which impeded agglomeration. This shows the ability of the particles to act as viscosifier and stabilizing agent. The result agrees with earlier work of Yildirim et al. [36], in which they stated that small particles size is known to improve the rheology of emulsion.

The stability of RH-SPNF is extremely essential for its applicability in oil field reservoirs. Therefore, the determination of electrophoretic behaviour through zeta potential was conducted to determine the dispersal behaviour of RH-SNP. High zeta potential indicates that RH-SNP is electrically stable. Fig. 4 shows the zeta potential of RH-SNP. The zeta potential of -21.2 mV shows that RH-SNP was relatively stable. The stability was due to small size of the RH-SNP, which is consistent with the particles size distribution result (Fig. 3). Small particles are separated at low velocities due to gravitational forces which can decrease the movement of droplets, impede sedimentation and other instabilities [36]. The negative value of the zeta potential was due to increased dissociation of the silanol group on the surface of the SiO_2 particles. The good electron

Table 2 – XRD RH-SNP phases.

Phase name	Content (%)
Silicon dioxide (SiO_2)	97.83
Zeolite	2.16
Others	0.01

charge on the surface showed strong repellent forces among the particles. Thus, it demonstrates that repulsive forces were adequate to inhibit attraction between RH-SNP triggered by Brownian motion, through the mechanism of electrostatic repulsion, which prevented aggregation resulting in stabilization.

3.4. *Crystallization structure result*

The XRD result (Fig. 5) shows the presence of a broad peak at 2θ between 15 to 35°, and a sharp peak at 2θ = 22°, which confirms the presence of amorphous SiO_2 and crystalline SiO_2, respectively. The thermal treatment of RH generated a mixture of amorphous and crystalline SiO_2. The crystalline SiO_2 is evident by the sharp peak observed, which reveals the formation of tridymite structure [37]. The intensity peak at 44.5° indicates that a fraction of the amorphous phase was converted into crystalline phase of graphite structure [38]. This was due to leaching of the zeolite out of the amorphous phase, which agrees with prior work of Bansal et al. [39]. They reported leaching of biomolecules and protein out of the amorphous RH. Table 2 shows that RH-SNP contains about 97.83% of SiO_2. This indicates that RH has great potentials as an alternative source of SiO_2, and further confirms the purity and effectiveness of the method applied herein. The RC of RH-SNP was 26%. This could be due to the thermal heating of the RH. The result is consistent with previous study of Har et al. [40] where they reported a crystallinity of 22.18 – 32.58% at different temperatures. Similar result was reported in earlier work by Wang et al. [41] where they stated that RH-SNP are initially amorphous but the extended pyrolysis of the heated nanoparticles at 800 °C enhanced the crystallinity. Also, the increased crystallinity might be because of diffusion induced mechanism of RH-SNP crystallization. This is consistent with previous finding that ball milling strongly influences the kinetics of transformation of amorphous phase to crystalline phase [42]. With the increase in crystallinity, the RH-SNP can be processed to desirable shapes and possesses sufficient structural integrity which increases their industrial accessibility [21,41].

3.5. *Chemical structure and surface properties result*

To evaluate the chemical bonding of RH-SNP, the major chemical groups of RH-SNP were identified by FTIR (Fig. 6). The broad peak at 3200-3600 cm^{-1} corresponds to the stretching vibration of silanol hydroxyl group (Si—O—H). The peaks at 2974 cm^{-1} and 2843 cm^{-1} show —C—H group, indicating the organic surface and SiO_2 obtained in amorphous state [43]. The band at 1649 cm^{-1} shows the deformation of water molecules absorbed on the SiO_2 surface. The peaks at 1454 cm^{-1} and 1381 cm^{-1} were due to the —OH group, whereas the peak at 1273 cm^{-1} is attributed to the vibration mode of the SiO_2 network. The peak at 1085 cm^{-1} indicates the asymmetric stretching vibration of Si—O—Si [44]. The broad shoulder between 1045–877 cm^{-1} can be attributed to the vibration of tetrahedral SiO_4 coordination unit [45]. This shows that the chemical structure of SiO_2 was not affected by the synthesis method. The FTIR spectrum did not show the presence of other organic and inorganic materials, which confirms the high purity of the RH-SNP. This is because the alkaline earth cations (Fig. 2) created a non-bridging oxygen, thus enabling the re-organization of the SiO_2 network [46]. This agree with earlier study by Borouni et al. [42] where they stated that no other reaction has taken place in the mixture during ball milling thereby, only indication of crystalline SiO_2 is seen in the FTIR result. The result is consistent with the EDX (Fig. 2) and XRD (Table 2) results, which show a purity of 97.83%.

3.6. *Impact of RH-SNP on rheology of HPAM solution*

The effect of RH-SNP on rheology of HPAM was studied. Fig. 7 depicts the flow behaviour of RH-SPNF in comparison with HPAM at the same concentration (0.2 wt%). The concentration represents the critical concentration for nanoparticles and HPAM [12]. The viscosity of RH-SPNF was higher than HPAM solution at all shear rates. RH-SPNF and HPAM solution displayed pseudoplastic behaviour, which might be due to strong electrostatic hydrogen linkage between silanol group of RH-SNP (Fig. 6) and the HPAM amino group [12,13]. Also, the adsorption interaction between RH-SNP, which acted as crosslinkers, might be responsible for the trend. This is coherent with previous study of Corredor-Rojas et al. [47] where they reported that increased viscosity with addition of modified SiO_2 nanoparticles can be attributed to the crosslinking between the nanoparticles and the polymer chains through hydrogen bond or hydrophobic interaction. Although the bridges between RH-SNP molecules were not broken-down, they deteriorated gradually in shear field resulting in shear-thinning. RH-SPNF showed higher viscosity compared to HPAM at all shear rate. This was because of electroviscous negative charge on the surface of RH-SNP (Fig. 4) and the formation of stronger particle-particle hydrogen bonds compared to that formed by HPAM. The result is coherent with previous work of Shafiei-Sabet et al. [48], who reported that the rheological properties of cellulose nanocrystals vary due to their surface charge and ionic strength.

3.7. *Impact of RH-SNP on precipitation of HPAM solution*

Reservoir brine poses a serious problem on flow behaviour of injected HPAM. Therefore, the effect of RH-SNP on the salinity resistance of HPAM was investigated. The result (Fig. 8) shows that the viscosity of RH-SPNF and HPAM reduced as concentration of NaCl increased. This might be because of screening effect of Na^+, which reduced the repulsive energy and the hydrodynamic volumes of RH-SPNF and HPAM subsequently reducing viscosity [49,50]. Both RH-SPNF and HPAM still retained their pseudoplastic and shear-thinning behaviour as salinity increases. However, RH-SPNF showed higher viscosity compared to HPAM at the same concentration. This could be attributed to the interaction between the electrolyte and RH-SNP, which induced a bridging flocculation of RH-SNP and

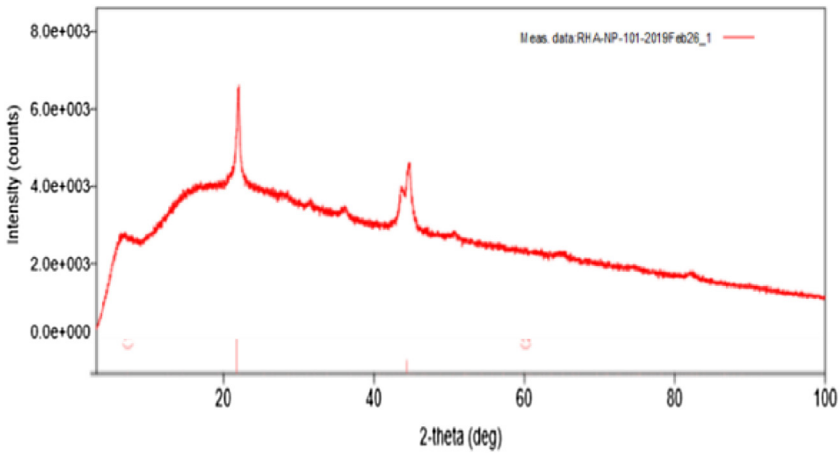

Fig. 5 – XRD of RH-SNP thermally treated at 700 °C.

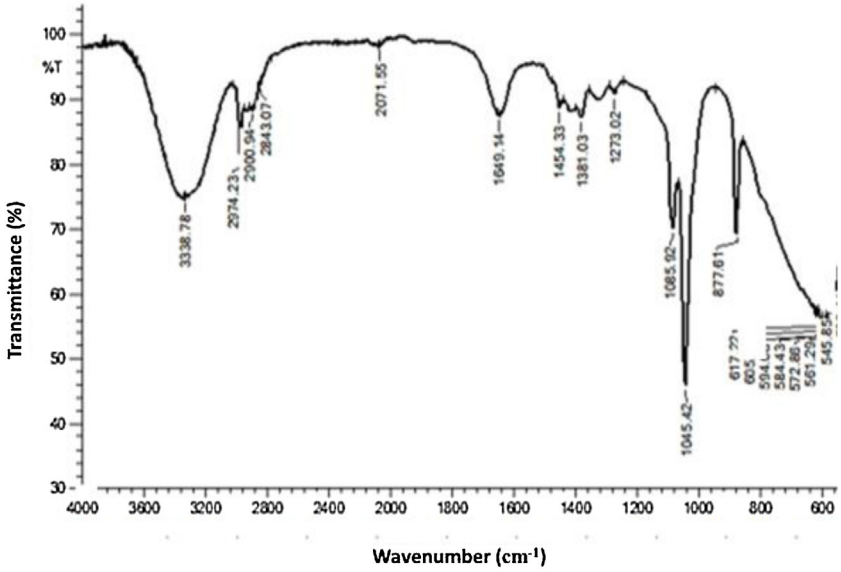

Fig. 6 – FTIR spectra for 0.1 wt% RH-SNP dispersion.

HPAM resulting to increased viscosity [51]. As cations of brine neutralize negative charge of HPAM, the adsorption interaction of RH-SNP on HPAM surface shielded the RH-SPNF from effect of electrolyte [12]. With RH-SPNF, there was interaction between oxygen atom on RH-SNP surface (Fig. 2) and Na^+ cations (ion-dipole) (Figure S6a). Hence, the nanoparticle shielded the HPAM molecules from precipitating. Additionally, the strong hydrogen bond created by the crosslinking of the RH-SNP and HPAM makes it resistant to degradation (Figure S6b). This agree with earlier study by Wu-Hua et al. [52] who stated that with the addition SiO_2 (with negative charge), the effect of cations on the HPAM polymer chain is weakened. This is because of the adsorption of cations between the HPAM and SiO_2 thus, the hydrodynamic volume of HPAM molecules and viscosity of the solution are increased and the salt resistance is improved. Whereas, the low viscosity of HPAM was because the Na^+ cations of the electrolyte and oxygen atom on anionic polyelectrolyte surface attacked the amide and carboxylate ions on HPAM molecules (Figure S6b), thereby diminishing the electrostatic repulsion within the polymer chain resulting in precipitation, loose of viscosity and degradation [13]. Similar result was reported by prior work of Wu-Hua et al. [52] where they stated that the repulsive force between HPAM chain makes the polymer form a loose structure in liquid phase and the reaction between the Na^+ from the brine and C=O from HPAM molecular chain led to reduction of viscosity. The reproducibility of the experimental results is shown by the error bar which indicates that the uncertainty is rather infinitesimal.

3.8. *Impact of RH-SNP on thermal degradation of HPAM*

Thermal degradation of a material is very important when determining the energy needed to overpower the activation energy of flow as material moves from one equilibrium to another. Fig. 9 shows the effect of temperature (26–80 °C) on the viscosity of RH-SPNF compared to HPAM solution at

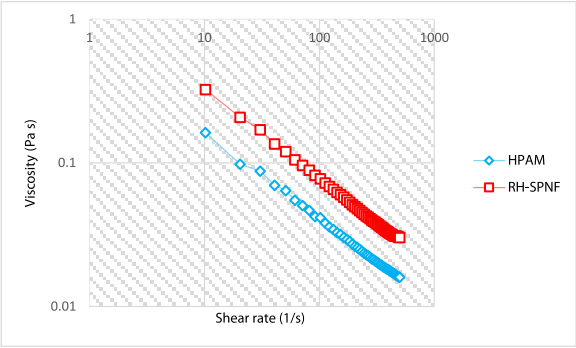

Fig. 7 – Effect of RH-SPNF on rheology of HPAM suspension.

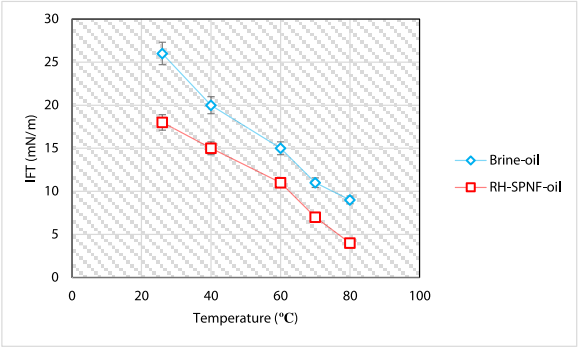

Fig. 10 – IFT of RH-SPNF in the presence of brine (2.2 wt%) at different temperature.

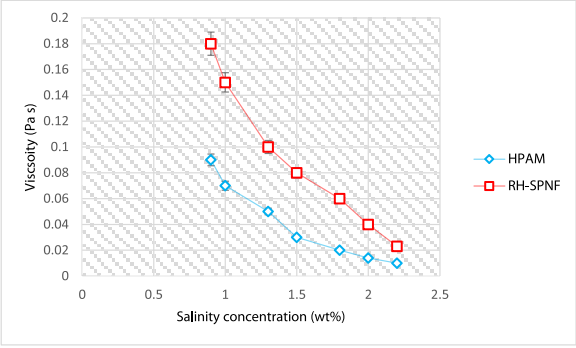

Fig. 8 – Effect of RH-SPNF on viscosity of HPAM solution as a function of salinity concentration.

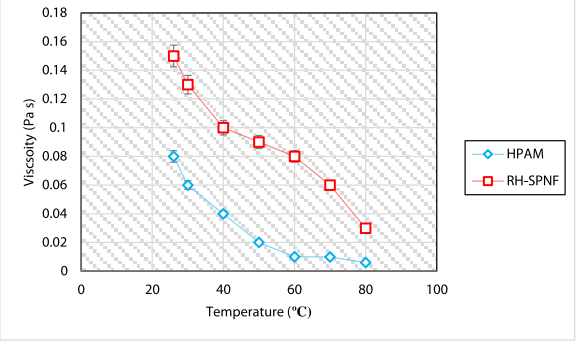

Fig. 9 – Effect of RH-SPNF on the viscosity of HPAM at different temperature.

the same concentration (0.2 wt%), with standard error bar almost the same. This signifies that the mean computed value estimated the true mean value of the experimental results. The results show that the viscosities of RH-SPNF were dependent on temperature. The viscosities of RH-SPNF and HPAM declined as temperature increased. This is adduced to increased mobility of HPAM particles as temperature increased, resulting in decline of intermolecular communication. It might have resulted in coiling, which led to decrease in viscosity. Also, at elevated temperature, hydrogen bond amongst the HPAM molecules becomes weak; this result to a fragile link between the molecular structure and decline in viscosity of HPAM [51]. However, in the case of RH-SPNF, as temperature increases, there was dihydroxylation of hydrogen bond on the silanol group that weakened the structure of RH-SPNF. This induces a hydrophobic nature and resulted in the decrease in viscosity [13]. Nevertheless, RH-SPNF still retained a higher viscosity compared to HPAM. This is because the increase in surface area of the RH-SNP resulted in an increase in its functionality which aids adsorption interaction with the polymer molecule. Hence, stronger hydrogen bond is formed between the nanoparticle and the polymer moieties which lessen the thermal impact on the suspension and increased the viscosity of the colloidal system [49,53]. This is consistent with previous study of Corredor-Rojas et al. [47] who reported that polymeric chain can be attached to more than one particle at a time, leading to the formation of a three-dimensional network of flocs.

3.9. *Impact of RHA-SPNF on IFT*

IFT between trapped oil and displacing fluid plays a significant role in oil recovery. Reducing IFT allows deformation of the O/W interface, which leads to improved oil recovery. Nanofluids have been reported to reduce IFT, but the interfacial properties strongly hinged on the quantity of surface-active agent which moves to the interface of O/W. Also, the movement of these surface-active agents from suspension to interface hinges on the medium temperature. Therefore, the impact of temperature (26–80 °C) on surface-active agents (from RH-SNP) at the interface of oil and brine (2.2 wt%) was studied. Fig. 10 shows the IFT of RH-SPNF compared to brine as a function of temperature. The result shows that there was a significant decrease in IFT in the presence of RH-SPNF compared to brine alone. It could be credited to the electrostatic interaction of RH-SPNF and brine in the bulk, which increases the dispersion of RH-SPNF to the interface of O/W [54]. The interactions between RH-SPNF in the presence of brine were found to be lower than those of brine alone (Fig. 10). This singularly confirms the formation of surface-active agent from electrostatic attraction between RH-SPNF and brine which could have significantly reduced O/W IFT compared to brine alone.

As the temperature of RH-SPNF increases, the liquid molecules have a higher kinetic energy. Hence, there was a

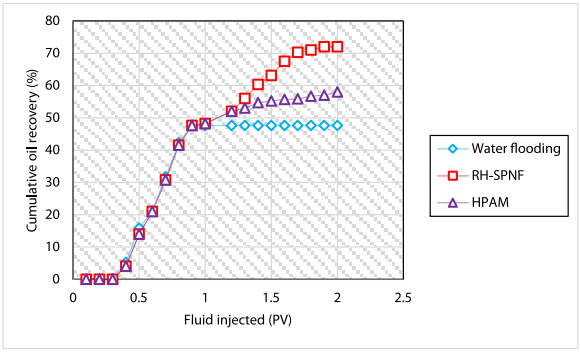

Fig. 11 – Cumulative oil recovery versus pore volume of injected fluids.

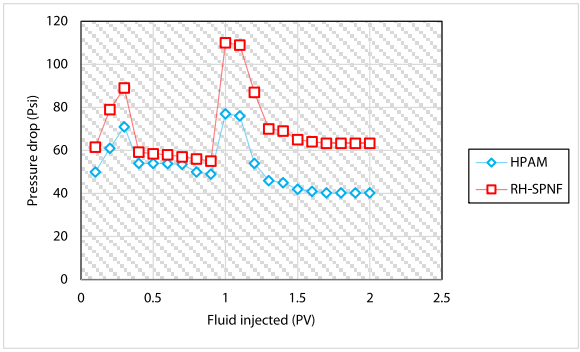

Fig. 12 – Pressure drop versus pore volume of injected EOR fluids.

rapid migration of RH-SPNF from the bulk to the O/W interface (Figure S7). This can be attributed to thermophoresis of the RH-SPNF, which is consistent with previous studies of Mahian et al. [55] and Agi et al. [56] where they reported that in nanofluid thermophoresis migrate particles from a region with higher temperature (hot zone) to region with lower temperature (cold zone). This led to a significant adsorption of RH-SNP at the interface, resulting in a charged electric double layer (EDL) which decreased the coating at the interface [57]. This weakens the cohesive energy and expands the intermolecular energies at the interface thereby reducing IFT of RH-SPNF. The standard error of the IFT and temperature were determined for two tests. The error bars were used to determine the positive and negative standard error from the mean of IFT and temperature. It was observed from the error bar (Fig. 10) that the results show good parallelism, indicating that the experimental results are reliable and reproducible.

3.10. *Oil displacement results*

To determine the stability, effective treatment methods and the potentials of RH-SPNF for EOR, series of core flooding experiments were performed to mimic water flooding and polymeric nanofluid flooding of a Sarawak oil field. The cumulative oil recovery recorded for each of the secondary and tertiary recovery modes are presented in Fig. 11. Water flooding recovered 48% OOIP, which signifies that sufficient quantity of oil was bypassed. Tertiary recovery was initiated and oil recovery increased by 10% and 24% with HPAM and RH-SPNF, respectively. The relative standard error of the oil displacement experiment is determined as 0.25%. This implies that the uncertainty of the experiment is infinitesimal and confirms the repeatability of the experiments. The presence of polymer blocked the permeable channels created during water flooding and recovered additional oil by mechanism of disproportionate permeability reduction [58]. Hence, the viscous fingers generated during the waterflooding process was minimised and/or eradicated. RH-SPNF had a higher recovery performance due to the shielding effect of the nanoparticles on the polymer performance, which inhibited degradation of its molecules at high temperature and salinity conditions. The improved rheological performance of RH-SPNF facilitated the mobilization of the initially bypassed oil and ensured better

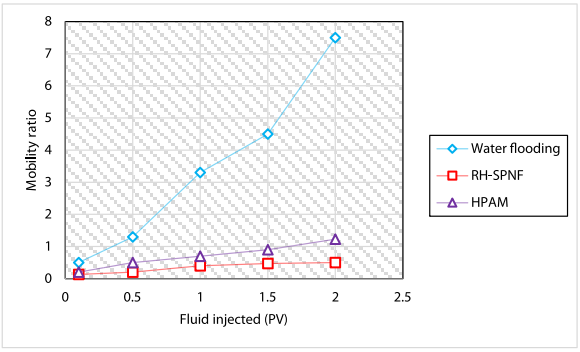

Fig. 13 – Mobility ratio versus pore volume of injected fluids.

conformance control. Additionally, the higher recovery of RH-SPNF could be attributable to reduction in IFT at O/W interface due to surface activity of the RH-SNP, which might have caused an enhancement in pore scale displacement efficiency. The core flooding result further confirms the enhanced properties of RH-SPNF at high salinity (2.2 wt%) and HPHT (3000 psi, 120 °C) reservoir conditions.

The pressure drop profile shows a good relationship with recovery result (Fig. 12). When waterflood commenced, there was a rise in pressure drop, followed by a decline until it became constant. The reason for the declining trend was due to the high mobility of water compared to oil, which was evident as breakthrough time saw the pressure drop remain constant. A favourable type of displacement will occur if:

$$\frac{k_{rw}\,\mu_w}{k_{ro}\mu_o} = M \leq 1 \quad (4)$$

where M is mobility ratio, μ_o is viscosity of oil (mPa s), μ_w is viscosity of water (mPa s), k_{ro} and k_{rw} are end point relative permeabilities of oil and water respectively, (*mD*). Mobility ratio was determined using the method of Bamidele et al. [59]. It was observed that the mobility ratio of water flooding approaches unity faster than that of HPAM and RH-SPNF, respectively (Fig. 13). This might have resulted in bypassing of oil and consequently early breakthrough in the water flooding, which is consistent with pressure drop profile (Fig. 12). The delay in approaching unity for HPAM and RH-SPNF signifies that the oil viscosity variation was less than their water

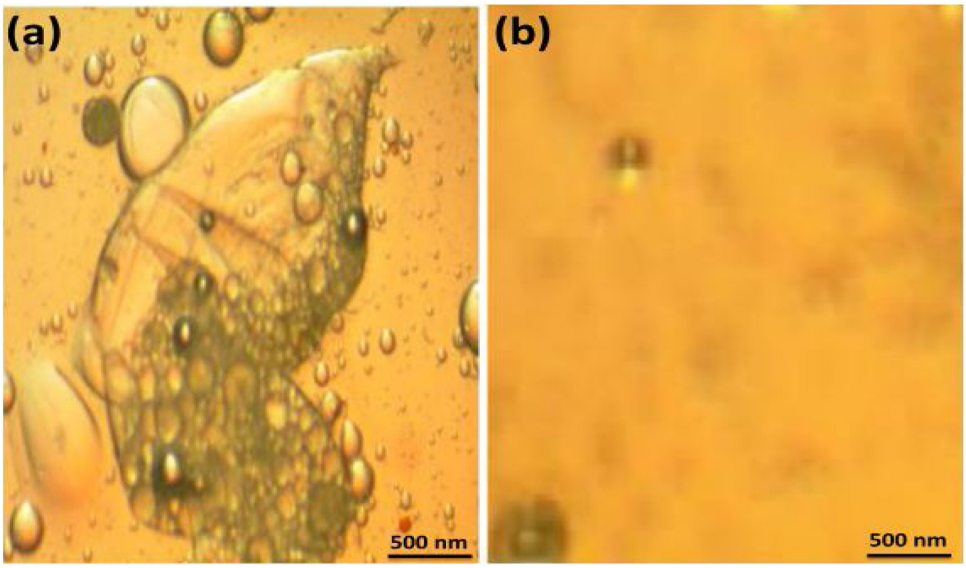

Fig. 14 – Microscopic image of emulsion generated during (a) HPAM flooding showing large drop sizes, (b) RH-SPNF flooding showing small size droplets.

viscosity variation, thereby resulting in a favourable mobility. EOR also saw an increase in pressure drop profile. The rise during tertiary recovery was due to their improved viscosity compared to water [58].

Increase in pressure drop as RH-SPNF was introduced demonstrates that the polymeric nanofluids lowered the capillary forces holding the oil in pore spaces [60]. The pressure drops remained very high even at elevated temperature, which confirms that RH-SPNF was still stable and oil displacement efficiency was still very active at 120 °C, which resulted to increased oil recovery. As the nanofluids imbibe into the sandstone core to expel trapped oil, the pressure profile began to build leading to the formation of O/W emulsion. This agrees with earlier work of Pei et al. [61] where they stated that O/W emulsion enhanced the sweep efficiency by blocking the channel created by water and lowered the oil mobility. The emulsion generated was examined with an Amscope microscope (Fig. 14). Emulsions generated by HPAM (Fig. 14a) showed large drops sizes with high-level of coalescence compared to RH-SPNF emulsion (Fig. 14b), which has small diameter droplets, which signifies stability of the emulsion over a long period [62]. This agrees with the recovery results as this singular phenomenon might be one of the reasons for the higher recovery of RH-SPNF compared to HPAM. The result also confirmed the ability of RH-SPNF to withstand high temperature compared to HPAM, which is consistent with the thermal degradation results (Fig. 9).

4. Energy and cost estimation

The energy estimation of RH-SNP (Table 3) was a thousand times less than SiO_2 or fumed quartz extracted from sand which utilizes the electric arc method (1400 kwh) and one hundred times less than TRACI method (217 kwh) available in GABi software data base [63]. Also, SiO_2 extraction from sand utilizes non-renewable natural resources, which can affect the biodiversity and subsequently have huge environmental impact on the mined area in a long run. This environmental impact can be avoided if RH is used as a raw material. RH was obtained free of charge as a waste product. The cost estimation of this study (Table 3) suggests that the preparation method of RH-SNP was cost-effective compared to facial route method (US$36.2) [64] and chemical treatment method (US$63.03–92.98) [65]. The cost may reduce further if RH-SNP is produced at industrial scale. Therefore, the low energy utilization, use of low-cost raw material, low investment and operation cost make RH-SNP and the extraction method an appropriate substitute to commercially available SiO_2 nanoparticles.

Table 3 – Energy and cost estimation for RH-SNP synthesis per kilogram (kg).

Materials and Process	Energy (kwh)	Cost (US$)/kg
RH	-	–
Ethanol	-	6.6/litre
Heating	1.5	0.0825
Size reduction	5.25	0.0289
Drying	12.5	0.701
Miscellaneous	-	10
Total	19.25	18.1549

Note: Market value of SiO_2 nanoparticle = US$185/kg (https://www.us-nano.com/inc/sdetail/408)

5. Conclusions

This study was conducted to produce environmentally friendly and cost-effective SiO_2 nanoparticles and test their applicability as a novel fluid for EOR. The properties of RH-SNP with its size distribution were studied by FESEM and DLS. The

influence of the process variables was studied. FTIR was used to determine the functional groups of RH-SNP, whereas EDX and XRD separated and identified the purity of the RH-SNP components. The effect of RH-SNP on the thermal degradation of HPAM and EOR mechanisms was related to the oil displacement ability of the RH-SPNF. Based on the results of this study, the following conclusions were reached.

1 The wet milling technique was effective in producing RH-SNP of size ranges 43.9–59.5 nm through the mechanism of nucleation, growth, capillary effect, Brownian motion and coalescence. EDX and XRD confirm the presence of SiO_2 and purity of RH-SNP, respectively.
2 The particles size distribution shows monomodal distribution and the zeta potentials reveal that RH-SNP solution was stable. This shows that RH-SNP could be used as a viscosifier and stabilizer.
3 The RH-SNP inhibited the precipitation and thermal degradation of oilfield HPAM due to their shielding effect.
4 The impact of electrostatic attraction was foremost than the effect of electrostatic repulsion in decreasing IFT. The IFT of RH-SPNF showed a monotonic trend with increase in temperature.
5 About 24% incremental oil recovery was achieved with the use of RH-SPNF. The microscopic image of the emulsion generated shows stability of the emulsion over a long period and confirmed the ability of RH-SPNF to withstand high temperature degradation compared to HPAM.
6 Therefore, the low energy utilization, use of low-cost raw material, low investment and operation cost make RH-SNP and the extraction method an appropriate substitute to commercially available SiO2 nanoparticles.

Funding Source

All sources of funding should also be acknowledged, and you should declare any involvement of study sponsors in the study design; collection, analysis and interpretation of data; the writing of the manuscript; the decision to submit the manuscript for publication. If the study sponsors had no such involvement, this should be stated.

Conflict of interest

The authors have no conflict of interest.

Acknowledgements

The authors would like to thank the Ministry of Higher Education (MOHE), Malaysia and Universiti Teknologi Malaysia for supporting this research through Research Management Grants Vot. No. R.J130000.3551.07G52, R.J130000.3551.06G68 & 06G69, R.J130000.2451.08G93, R.J 130000.3051.01M99, R.J 130000.7851.5F030 and R.J 130000.7351.4B545.

Appendix A. Supplementary data

Supplementary material related to this article can be found, in the online version, at doi:10.1016/j.jmrt.2020.08.112.

REFERENCES

[1] Abbas A, Moslemizadeh A, Sulaiman WR, Jaafar MZ, Agi A. An Insight into di-chain surfactant adsorption onto sandstone minerals under different salinity-temperature conditions: chemical EOR applications. Chem Eng Res Des 2020;153:657–65.
[2] Gbadamosi A, Junin R, Manan M, Agi A, Oseh J. Nanotechnology application in chemical enhanced oil recovery: current opinion and recent advances. Intechopen 2019:1–23.
[3] Tumba J, Agi A, Gbadamosi A, Junin R, Abbas A, Rajaei K, Gbohinbor J. Lignin as a potential additive for minimizing surfactant adsorption on clay minerals in different electrolyte concentration. In: SPE-198713-MS presented at SPE annual international conference and exhibition. 2019. p. 1–23.
[4] Pope GA. Recent developments and remaining challenges of enhanced oil recovery. J Pet Technol 2011;63(07):65–8.
[5] Saboorian-Jooybari H, Dejam M, Chen Z. Heavy oil polymer flooding from laboratory core floods to pilot tests and field applications: half-century studies. J. Pet. Sci. Eng 2016;142:85–100.
[6] Gbadamosi AO, Junin R, Manan MA, Yekeen N, Agi A. Hybrid suspension of polymer and nanoparticles for enhance oil recovery. Polym Bull 2020;76:6193–230.
[7] Maghzi A, Mohebbi A, Kharrat R, Ghazanfari MH. An experimental investigation of silica nanoparticles effect on the rheological behavior of polyacrylamide solution to enhance heavy oil recovery. Pet. Sci. Technol 2013;31:500–8.
[8] Lai N, Guo N, Zhou N, Xu Q. Shear resistance properties of modified nanoSiO_2/AA/AM copolymer oil displacement agent. Energies 2016;9:1037.
[9] Hu Z, Haruna M, Gao H, Nourafkan E, Wen D. Rheological properties of partially hydrolyzed polyacrylamide seeded by nanoparticles. Ind. Eng. Chem. Res 2017;56:3456–63.
[10] Abdullahi MB, Rajaei K, Junin R, Bayat AE. Appraising the impact of metal-oxide nanoparticles on rheological properties of HPAM in different electrolyte solution for enhanced oil recovery. J Pet Sci Eng 2019;172:1057–68.
[11] Haruna MA, Pervaiz S, Hu Z, Nourafkan E, Wen D. Improved rheology and high-temperature stability of hydrolyzed polyacrylamide using graphene oxide nanosheet. J Appl Polym Sci 2019;47582:1–13.
[12] Gbadamosi A, Junin R, Manan M, Agi A, Oseh J, Usman J. Synergistic application of aluminium oxide nanoparticles and oilfield polyacrylamide for enhanced oil recovery. J Pet Sci Eng 2019;182:106345.
[13] Gbadamosi A, Junin R, Manan M, Agi A, Oseh J, Usman J. Effect of aluminium oxide nanoparticles on oilfield polyacrylamide: rheology, interfacial tension, wettability and oil displacement studies. J Mol Liq 2019;296:111863.
[14] Piana G, Ricciardi M, Bella F, Cucciniello R, Proto A, Gerbaldi C. Poly(glycidyl ether)s recycling from industrial waste and feasibility study of reuse as electrolytes in sodium-based batteries. Chem Eng J 2020;382:122934.
[15] Dang C, Huang Chen Y, Zhou S, Feng X, Chen G, Dai F, Qi H. Direct dissolution of cellulose in NaOH/Urea/α-Lipoic acid

aqueous solution to fabricate all biomass-based nitrogen, sulfur dual-doped hierarchical porous carbon aerogels for supercapacitors. ACS Appl Mater Interfaces 2020;12:21528–38.
[16] Bella F, Chiappone A, Nair JR, Meligrana G, Gerbaldi C. Effect of different green cellulosic matrices on the performance of polymeric dye-sensitized solar cells. Chem Eng Trans 2014;41:211–6.
[17] Zolin L, Nair JR, Beneventi D, Bella F, Destro M, Jagdale P, Cannavaro I, Tagliaferro A, Chaussy D, Geobaldo F, Gerbaldi C. A simple route toward next-gen green energy storage concept by nanofibres-based self-supporting electrodes and a solid polymeric design. Carbon 2016;107:811–22.
[18] Bella F, Porcarelli C, Mantione D, Gerbaldi C, Barolo C, Gratzel M, Mecerreyes D. A water-based and metal-free dye solar cell exceeding 7% efficiency using cationic poly(3,4-ethylenedioxythiophene) derivative. Chem Sci 2020;11:1485.
[19] Fagiolari L, Bella F. Carbon-based materials for stable, cheaper and large-scale processable perovskite solar cells. Energy Environ Sci 2019;12:3437–72.
[20] Bella F, Galliano S, Piana G, Giacona G, Viscardi G, Gratzel M, Barolo C, Gerbaldi C. Boosting the efficiency of aqueous solar cells: a photoelectrochemical estimation on the effectiveness of $TiCL_4$ treatments. Electrochim Acta 2019;302:31–7.
[21] Fang D, Zhou J, Sheng L, Tang W, Tang J. Juglone bonded carbon nanotubes interweaving cellulose nanofibers as self-standing membrane electrodes for flexible high energy supercapacitors. Chem Eng J 2020;396:125325.
[22] Agi A, Junin R, Gbadamosi A. Mechanism governing nanoparticles flow behaviour in porous media: insight for enhanced oil recovery applications. Int Nano Lett 2018;8(2):49–77.
[23] Wei B, Li Q, Ning J, Wang Y, Sun L, Pu W. Macro and micro scale observation of a surface functionalized nanocellulose based on aqueous nanofluid in chemical enhanced oil recovery (C-EOR). Fuel 2019;236:1321–33.
[24] Riveros H, Garza C. Rice husks as a source of high purity. J Cryst Growth 1986;75(1):126–31.
[25] Jie CK, Jaafar MZ, Wan Sulaiman WR. Foam stability performance enhanced with rice husk ash nanoparticles. J Teknol 2019;81(4):87–96.
[26] Agi A, Junin R, Gbadamosi A. Tailoring of nanoparticles for chemical enhanced oil recovery activities: a review. Int. J. Nanomanufacturing 2020;16(2):107–47.
[27] Maghzi A, Kharrat R, Mohebbi A, Ghazanfari MH. The impact of silica nanoparticles on the performance of polymer solution in presence of salts in polymer flooding for heavy oil recovery. Fuel 2014;123:123–32.
[28] Agi A, Junin R, Alqatta AYM, Gbadamosi A, Yahya A, Abbas A. Ultrasonic ultrafiltration process for the emulsification of oil field produced water treatment. Ultrason Sonochem 2019;51:214–22.
[29] Nara S, Komiya T. Studies on the relationship between water saturated state and crystallinity by the diffraction method for moistened potatoes starch. StarchStark 1983;35(12):407–10.
[30] Rovani S, Santos J, Corio P, Fungaro D. Highly pure silica nanoparticles with high adsorption capacity obtained from sugarcane waste ash. ACS Omega 2018;3:2618–27.
[31] Agi A, Junin R, Gbadamosi A, Abbas A, Azli NB, Oseh J. Influence of nanoprecipitation on crystalline starch nanoparticle formed by ultrasonic assisted weak-acid hydrolysis of cassava starch and the rheology of their solutions. Chem Eng Process 2019;142:107556.
[32] Zhang Z, Wang Z, He S, Wang C, Jin M, Yin Y. Redox reaction induced Ostwald ripening for size- and shape-focusing of palladium nanocrystals. Chem Sci 2015;6(9):5197–203.
[33] Rades S, Hodoroaba V, Salge T, Wirth T, Lobera MP, Labrador RH, Natte K, Behnke T, Gross T, Unger WE. High-resolution imaging with SEM/T-SEM, EDX and SAM as a combined methodical approach for morphological and elemental analyses of single engineered nanoparticles. RSC Adv 2014;4:49577–87.
[34] Ngouangna EN, Manan MA, Oseh JO, MNAM Norddin, Agi A, Gbadamosi AO. Influence of (3–Aminopropyl) triethoxysilane on silica nanoparticle for enhanced oil recovery. Mol Liq 2020;315:113740.
[35] Wang H, Mustaffar A, Phan AN, Zivkovic V, Reay D, Law R, Boodhoo K. A review of process intensification applied to solids handling. Chemical Eng Process 2017;118:78–107.
[36] Yildirim M, Sumnu G, Rheology Sahin S. Particle-size distribution, and stability of low-fat mayonnaise produced via double emulsion. Food Sci Biotechnol 2016;25(6):1613–8.
[37] Fernandez IJ, Sanchez FAL, Jurado JR, Kieling AG, Rocha TLAC, Moraes CAM, Sausa VC. Physical, chemical and electric characterization of thermally treated rice husk ash and its potential application as ceramic raw material,. Adv Powder Technol 2017;28(4):1228–36.
[38] Kenes K, Yerdos O, Zulkhair M, Yerlan D. Study on the effectiveness of thermally treated rice husks for petroleum adsorption. J Non Cryst Solids 2012;358(22):2964–9.
[39] Bansal V, Ahmad A, Sastry M. Fungus-mediated biotransformation of amorphous silica in rice husk to nanocrystalline silica,. J. Am. Chem. Soc 2006;128:14059–66.
[40] Har N., Irzaman, Irmansyah. Crystallinity and Electrical Properties of Silicon dioxide (SiO2) from Rice Straw. AIP Conference Proceedings; https://doi.org/10.1063/1.5141641.
[41] Wang W, Martin JC, Fan X, Han A, Luo Z, Sun L. Silica nanoparticles and frameworks from rice husk biomass. ACS Appl. Mater. Interfaces 2012;4:977–81.
[42] Borouni M, Niroumand B, Maleki A. A study on crystallization of amorphous nano silica particles by mechanical activation at the presence of pure aluminium. J Solid State Chem 2018;263:208–15.
[43] Le VH Thuc CNH, Thuc HH. Synthesis of silica nanoparticles from vietnamese rice husk by sol-gel method. Nanoscale Res Lett 2013;8:58.
[44] Imoisili PE, Ukoba KO, Jen T. Green technology extraction and characterisation of silica nanoparticles from palm kernel shell ash via sol-gel. J Mater Res Technol 2020;9(1):307–13.
[45] Wang W, Martin JC, Zhang N, Ma C, Han A, Sun L. Harvesting silica nanoparticles from rice husks. J Nanopart Res 2011;13:6981–90.
[46] Drisko GL, Carretero-Genevrier A, Perrot A, Gich M, Gàzquez J, Rodriguez-Carvajal J, Favre L, Grosso D, Boissière C, Sancheza C. Crystallization of hollow mesoporous silica nanoparticles. ChemComm 2012;00:1–3.
[47] Corredor-Rojas LM, Hemmati-Sarapardeh A, Husein MM, Dong M, Main BB. Rheological behavior of surface modified silica nanoparticles dispersed in partially hydrolyzed polyacrylamide and xanthan gum solutions: experimental measurements, mechanistic understanding, and model development. Energy Fuel 2018;32(10):10628–38.
[48] Shafiei-Sabet S, Hamad WY, Hatzikiriakos S. Rheology of nano-crystalline cellulose aqueous suspensions. Langmuir 2012;28(49):17124–333.
[49] Agi A, Junin R, Arsad A, Abbas A, Gbadamosi A, Azli NB, Oseh J. Ultrasonic-assisted weak-acid hydrolysis of crystalline starch nanoparticles for chemical enhanced oil recovery. Int J Biol Macromol 2020;148:1251–71.
[50] Agi A, Junin R, Abbas A, Gbadamosi A, Azli NB. Effect of dynamic spreading and the disperse phase of crystalline starch nanoparticles in enhancing oil recovery at reservoir condition of a typical sarawak oil field. Appl Nanosci 2020;10(1):263–79.

[51] Maurya NK, Mandal A. Studies on the behaviour of suspension of silica nanoparticles in aqueous polyacrylamide solution for application in enhanced oil recovery. Petrol Sci Technol 2016;34(5):429436.
[52] Wu-Hua C, Ye-Fei W, Zhen-Pei HE, Ming-Chen D. Stability, rheology and displacement performance of nano-SiO2/HPAM/NaCl dispersion systems. J Fuel Chem Technol 2020;48(5):568–76.
[53] Esfe MH, Saedodin S, Mahian O, Wongwises S. Efficiency of ferromagnetic nanoparticles suspended in ethylene glycol for application in energy devices: effects of particle sizes, temperature and concentration. Int Commun Heat Mass 2014;58:138–46.
[54] Yekeen N, Padmanabhan E, Idris AK. synergetic effect of nanoparticles and surfactant on n-decane-water interfacial tension and bulk foam stability at high temperature. J Petrol Sci Eng 2019;179:814–30.
[55] Mahian O, Kolsi L, Amani M, Estelle P, Ahmadi G, Kleinstreuer C, Marshall JS, Siavashi M, Taylor RA, Niazmand H, Wongwises S, Hayat T, Kolanjiyil A, Kasaeian A, Pop I. Recent advances in modeling and simulation of nanofluid flows-part i: fundamentals and theory. Phys Rep 2019;790:1–48.
[56] Agi A, Junin J, Gbadamosi A, Manan M, Jaafar MZ, Abdullah MO, Arsad A, Azli NB, Abdurrahman M, Yakasai F. Comparing natural and synthetic polymeric nanofluids in a mid-permeability sandstone reservoir condition. J Mol Liq 2020;317:113947.
[57] Bera A, Mandal A, Guha B. Synergic effect of surfactant and salt mixture on interfacial tension reduction between crude oil and water in enhanced oil recovery. J. Chem. Eng. Data 2014;59(1):89–96.
[58] Kumar N, Mandal A. Surfactant stabilized oil-in-water nanoemulsion: stability, interfacial tension and rheology study for enhanced oil recovery application. Energy Fuels 2014;32(6):6452–66.
[59] Bamidele A, Fadairo A, Falode A. Endpoint mobility ratios for vertical and horizontal wells with incidence of scale deposition. Open Petrol Eng J 2009;2:17–23.
[60] Dong M, Ma S, Liu Q. Enhanced heavy oil recovery through interfacial instability: a study of chemical flooding for brintnell heavy oil. Fuel 2009;88:1049–56.
[61] Pei H, Zhang G, Ge J, Jin I, Ma C. Potential of alkaline flooding to enhance heavy oil recovery through water-in oil emulsion. Fuel 2013;104:272–8.
[62] Agi A, Junin R, Abdullah MO, Jaafar MZ, Arsad A, Wan Sulaiman WR, Norddin MNA, Abdurrahman M, Abbas A, Gbadamosi A, Azli NB. Application of polymeric nanofluid in enhancing oil recovery at reservoir condition. J Petrol Sci Eng 2020;194:107476.
[63] Joglekar SN, Kharkar RA, Mandavgane SA, Kulkarni BD. Process development of silica extraction from RHA: a cradle to gate environmental impact approach. Environ Sci Pollut R 2018, http://dx.doi.org/10.1007/s11356-018-3648-9.
[64] Hossain SK, Mathur L, Bhardwaj A, Roy PK. A facile route for the preparation of silica foams using rice husk ash. Int J Appl Ceram Technol 2019:1–9.
[65] Nayak PP, Nandi S, Datta AK. Comparative Assessment of Chemical Treatments on Extraction Potential of Commercial Grade Silica from Rice Husk. Engineering Reports 2019, http://dx.doi.org/10.1002/eng2.12035.